**Article**

# Body-worn and self-powered flexible optoelectronic device for metronomic photodynamic therapy

Check for updates

Jianhong Zhang[1,5], Xinhui Mao [2,5], Qingyan Jia [1,3] ✉, Renhao Nie[1], Yangyang Gao[2], Kai Tao [2] ✉, Honglong Chang[2], Peng Li [1] ✉ & Wei Huang [1,3,4] ✉

Photodynamic therapy (PDT) as a clinical method relies on appropriate light delivery to activate photosensitizers, usually necessitates the utilization of cumbersome surgical instruments and high irradiation intensity, along with the requirement for hospitalization. To extend the applicability of PDT beyond hospital for better patient mobility, we design a wearable and self-powered metronomic PDT (mPDT) system for chronic wound infection treatment. A flexible alternative current electroluminescent (ACEL) device is constructed through sandwiching an emissive layer between conductive hydrogel electrodes. This ACEL device works as a therapeutic patch by loading photosensitizer (PS) in its bottom hydrogel electrode, thus aviods the intravenous administration to patients. Under the triboelectric nanogenerator generated AC pulse, the electroluminescence produced from emissive layer can be absorbed by the PS-loaded electrode to generate reactive oxygen species for mPDT. Benefited from its arbitrary tailorability, this device can be customized into on-demand shapes and sizes. Using diabetic infected wound as a model condition, this ACEL mPDT device effectively eliminates drug-resistant bacteria and accelerates wound healing. Thus, the body-worn optoelectronic device successfully avoids the utilization of extracorporeal physical light and power sources, providing a promising strategy for convenient, user-friendly, and prolonged treatment of superficial diseases.

Photodynamic therapy (PDT) as a noninvasive and high spatial-temporal selective technology that generates biocidal reactive oxygen species (ROS) under light excitation, has been adopted in clinical practices for the treatment of various diseases such as dermatosis, cancer, as well as bacterial infection[1–4]. Unfortunately, large-scale surgical optical instruments are indispensable for conventional PDT, resulting in their professional operations restricted in hospitals or clinics that is unsuitable for chronic disease managements[5–7]. On such condition, high irradiation intensities are usually inevitable for PDT to reduce hospital length of stay. But the intense illumination may lead to a variety of side effects including pain, burn, and pustular formation, even induce carcinogenesis under serious circumstance[8]. To improve its safety and reliability, metronomic photodynamic therapy (mPDT) with reduced-dose intermittent irradiation that is

applicative for continuous and long-term treatment has emerged in recent years[9–11]. However, current reported extracorporeal mPDT equipments based on conventional light sources (such as diode laser and light emitting diode array) are difficult to fit the human body and cause discomfort to patients during prolonged treatments[12]. Therefore, it is crucial to construct lightweight, portable, and wearable optoelectronic devices for personalized PDT.

Electroluminescent (EL) devices have been widely explored in electronic skin, soft robot, imaging, etc[13–17]. Their successful exploration in biomedical system renders a candidate as the excitation source for PDT. Alternating current electroluminescence (ACEL) is a light-emitting technique with low energy consumption[18–20]. The insulating dielectrics of ACEL devices are inessential for band matching, making them suitable for low-cost

[1]Frontiers Science Center for Flexible Electronics (FSCFE), Xi'an Institute of Flexible Electronics (IFE) and Xi'an Institute of Biomedical Materials and Engineering (IBME), Northwestern Polytechnical University, 127 West Youyi Road, Xi'an, China. [2]Ministry of Education Key Laboratory of Micro and Nano Systems for Aerospace, School of Mechanical Engineering, Northwestern Polytechnical University, 127 West Youyi Road, Xi'an, China. [3]Key laboratory of Flexible Electronics of Zhejiang Province, Ningbo Institute of Northwestern Polytechnical University, 218 Qingyi Road, Ningbo, China. [4]School of Flexible Electronics (SoFE) and Henan Institute of Flexible Electronics (HIFE), Henan University, 379 Mingli Road, Zhengzhou, China. [5]These authors contributed equally: Jianhong Zhang, Xinhui Mao. ✉e-mail: iamqyjia@nwpu.edu.cn; taokai@nwpu.edu.cn; iampli@nwpu.edu.cn; iamdirector@fudan.edu.cn

displays and large-area flexible equipments applications[21]. Owing to the frequent overturning of the applied electric field, charge accumulation could be effectively avoided, thus improving their power efficiency and service life[22,23]. In the development of power supply devices, energy harvesters as self-sustained power sources have the ability to capture biomechanical energy and convert it into electricity, providing a promising green energy system in comparison to the conventional batteries[24–29]. Based on triboelectricfication and electrostatic induction coupling, the triboelectric nanogenerator (TENG) exhibits unique advantages in easy manufacturing, high energy conversion efficiency, as well as environmental friendliness[30–32]. Particularly, TENG with inherent AC output capability achieves a appropriate power supply to drive various wearable devices, as well as ACEL for warning or lighting[33–35].

In this work, we designed a wearable self-powered biomedical device for personalized mPDT, based on a fully flexible and customizable ACEL device loaded with photosensitizer (PS) under the driving of TENG (Fig. 1a). This ACEL mPDT device was prepared by sandwiching an emissive layer composed of ZnS:Cu,Al phosphor doped polydimethylsiloxane (PDMS) between a conductive hydrogel electrode and another PS rose bengal (RB) loaded hydrogel electrode. And the origami-inspired TENG with light weight and long-term durability was chosen as the energy supply for mPDT. Our device significantly improves the convenience, serviceability, and patient compliance of conventional PDT device. Under the AC electric field, the metronomic electroluminescence could be emitted from emissive layer through the recombination of electrons and holes for extended periods of time. Benefited from the layer-by-laryer stack structure and the matching of photon release and absorption, the electroluminescence energy was efficiently absorbed by the PS-loaded layer to produce singlet oxygen ($^1O_2$) in situ for mPDT (Fig. 1b).

To confirm the curative effect of this wearable ACEL mPDT device, its antibacterial capability was assessed in an infected chronic wound model. The multidrug-resistant bacteria-infected chronic wounds have become an intractable challenge in clinical care that leads to poor quality of life, huge socio-economic burden, and increasing mortality. More than 6.5 million chronic non-healing wounds with evidence of bacterial infections are diagnosed annually in the United States alone[36]. Wounds are often in various irregular geometries but conventional optoelectronic devices are usually non-adjustable to such diversified shapes. Our ACEL mPDT device could be customized to arbitrary dimensions for cooperating the infected wounds with varying shapes and sizes that maintains consistent electroluminescence. Specifically, this ACEL mPDT device is insignificant phototoxic to skin tissue, making it suitable for wearable long-term mPDT. Meanwhile, the TENG as an energy harvester could power ACEL mPDT

device. As a demo example, it was embedded in the shoes to collect mechanical energy from human walking. Under the ACEL excitation, this therapeutic bioelectronic device exhibits excellent biocidal ROS generation capability that efficiently eradicates pathogenic microorganisms and promotes the chornic wound healing in vitro and in vivo. This integrated ACEL mPDT device presents a body-worn, self-powered, and long-term dynamic therapy that is unlimited to clinical settings, and achieves the on-demand customization for non-healing infected wounds.

## Results
### Design of the ACEL device for mPDT
A wearable optoelectronic device for continuous and prolonged mPDT was constructed based on flexible layered structure, in which an ACEL emissive layer was sandwiched between two conductive hydrogel electrodes (Fig. 2a, b). Owing to the potential side effects and psychological distress to patients, conventional methods of administering photosensitizers, such as intravenous, oral, and hypodermic injection, are inapplicable to chronic wound treatments[37,38]. The hydrogels have been employed as dressing for the delivery of drug in PDT of wound infection[39,40]. Therefore, we inventively incorporated PS into the bottom hydrogel electrode of the ACEL device, thereby enabling it to function as a therapeutic patch in contact with the diseased tissue. Due to the compact integration of the PS-loaded hydrogel electrode and ACEL emissive layer, the electroluminescence generated from the emissive layer could be directly transmitted to the hydrogel electrode for efficiently exciting PS molecule to generate biocidal ROS.

Owing to its stable chemical and optical properties, Cu, Al-doped zinc sulfide wurtzite phosphors (ZnS:Cu,Al) were selected as luminescent material for our ACEL device (Supplementary Fig. 1a, b). The ZnS:Cu,Al phosphors were blended with PDMS elastomer to form a flexible light-emitting composite film (Supplementary Fig. 2a). The dispersion of ZnS:Cu,Al phosphors in the emissive layer was confirmed by scanning electron microscope (SEM) and energy-dispersive X-ray spectroscopy (EDS) element analysis (Fig. 2c and Supplementary Fig. 2b, c). The SEM images indicated that ZnS:Cu,Al phosphors were compactly embedded in the PDMS film. Additionally, the phosphors' Zn, S, Cu, Al elements were observed to be uniformly distributed in the PDMS matrix composed of C, Si, and O, ensuring the desirable optical field of ACEL mPDT device. For the top and bottom electrodes, an ionic conductive polyacrylamide hydrogel (gel) with favorable light transmittance was selected (Supplementary Fig. 3a), and its conductivity was tunable by adjusting the ion concentration to fulfill the requirement of the ACEL device. In addition, the obtained sandwiched ACEL device exhibited full flexibility under distortion to satisfy



**Fig. 1 | Body-worn and self-powered ACEL mPDT device for wound infection treatments.**
**a** Schematic illustration of the human motion-driven therapeutic device. A user wears a flexible ACEL device (green square) for long-term metronomic photodynamic therapy. This sandwiched ACEL device emits green electroluminescence (emissive layer) that absorbed by the photosensitizer-loaded hydrogel electrode to generate $^1O_2$ in situ for effective eradication of pathogenic drug-resistant bacteria or fungi. And it can be powered by the self-powered nanogenerator (orange dots) that converts available mechanical energy from human movements (such as walking or flexing of joints) into electrical energy. **b** Mechanism diagram of the $^1O_2$ generation. Under an AC electric field, electroluminescence generated from the emissive layer based on the injection and recombination of electrons and holes is absorbed by the photosensitizer to produce $^1O_2$ through energy transfer process.
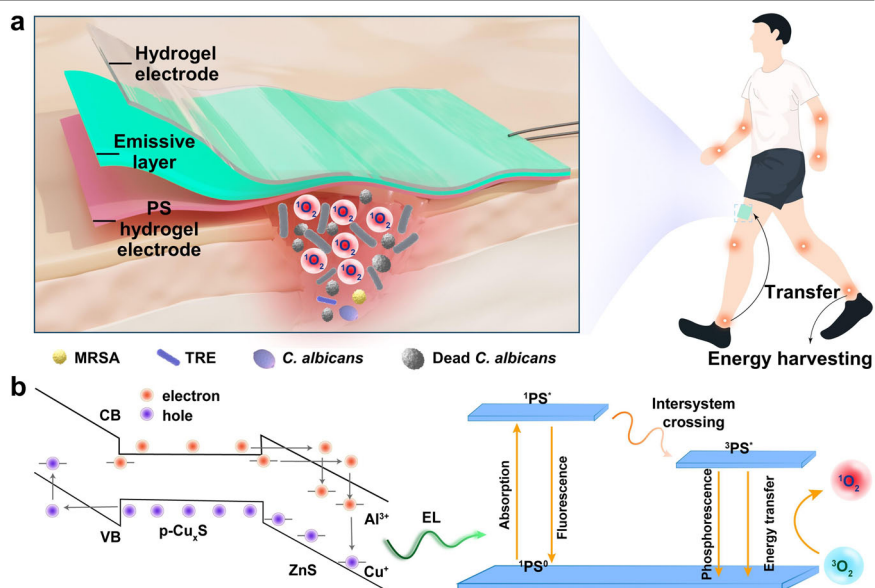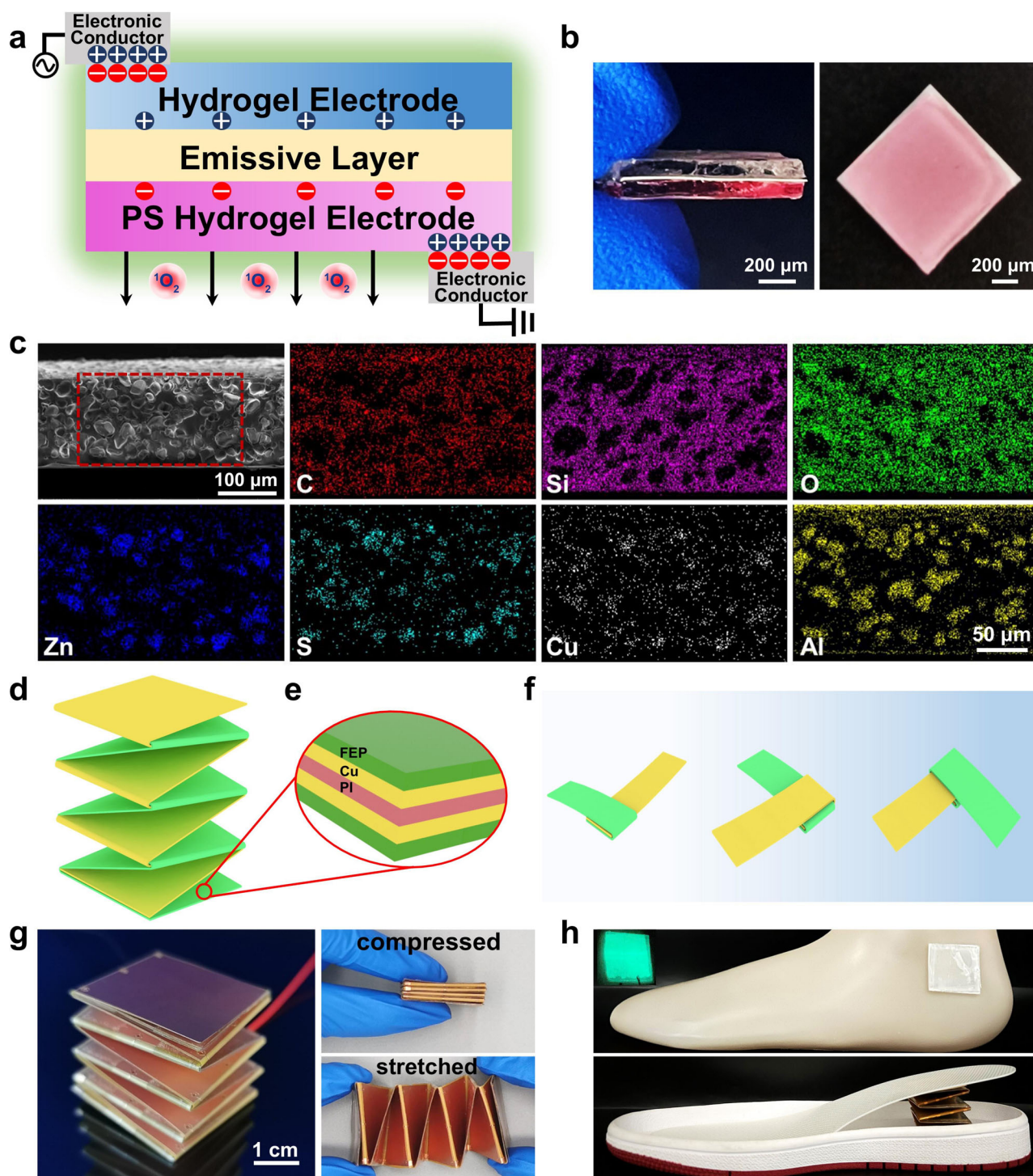
**Fig. 2 | Design of the self-powered ACEL mPDT device. a** Principle of the ACEL mPDT device. This sandwiched ACEL mPDT device includes the hydrogel electrode layer (top), emissive layer (middle), and PS hydrogel electrode layer (bottom), and it connects to the power through electronic conductor. Under the AC electric field, the emissive layer emits green electroluminescence, and then activates PS to generate $^1O_2$. **b** Photographs of the ACEL mPDT device (left: side view; right: top view). **c** SEM micromorphology and EDS element surface distribution of the emissive layer.

**d** Schematic diagram of the origami-inspired TENG. **e** Cross-sectional view of the FEP/Cu/PI/Cu/FEP layered structure. Green, yellow, and purple respectively represents FEP, Cu, and PI. **f** Preparation process of the TENG. **g** Photographs of the TENG at initial, compressed, and stretched state. **h** Demonstration model of the TENG-driven ACEL mPDT device. The TENG embedded in the shoes through energy harvesting can drive this ACEL mPDT device to emit green electroluminescence.

the demand of human motions (Supplementary Fig. 3b), rendering a comfortable and wearable optoelectronic device for patients.

The stable electrical double layers can form between the ionic hydrogel electrodes and electronic conductors when the ACEL device is connected to an AC power, leading to the behavior of the electrical double layers and

emissive layer in our ACEL device resembling that of three capacitors[41]. As depicted in the equivalent circuit illustrated in Supplementary Fig. 4, these capacitors are coupled in series and possess equal amounts of stored charges ($Q = C_1V_1 = C_2V_2 = C_3V_3$). The capacitance of the emissive layer is considerably smaller compared to the other electrical double layers due to the

separation of opposite polarity charges at nanometer-and millimeter-scales in electrical double layers and emissive layer, respectively[20]. Therefore, the applied voltage is concentrated on the emissive layer, resulting in the generation and acceleration of mobile electrons as well as excitation of phosphors.

## Fabrication of self-powered ACEL mPDT device

The operation of conventional optoelectronic devices is generally dependent on the extracorporeal power sources, which inevitably imposes restrictions due to factors such as limited battery lifespan, potential safety hazards, and risks associated with environmental pollution[42]. In addition, the bulky and inflexible design of external power source poses challenges in meeting the requirement for wearable therapeutic system, resulting in inconveniences and poor patient compliance over an extended period. And conventional small-size batteries with direct current output are incapable of driving this ACEL device. Due to the requirement for consistently intermittent power supply of our ACEL mPDT device over an extended period, the implementation of such powered system would cause discomfort. TENG, as a light-weight and durable power source, has the ability to convert available biomechanical energy from daily activities into electrical energy without excessive energy consumption, thereby providing an optimal power supply with comfortable wearability for activating the ACEL device[43–45].

As a bioenergy harvester for the ACEL mPDT system, the TENG was designed based on the folding of two strip electrodes[46], and its complete structure is illustrated in Fig. 2d. The electrode layers with stacked sandwich structures consisted of copper/polyimide/copper (50 μm/25 μm/50 μm). And one of the electrodes was affixed with fluorinated ethylene propylene (FEP) electret film on both its front and back surfaces for corona charging (Fig. 2e). In order to enhance the contact electrification, the surface of the FEP was subjected to ion beam etching, resulting in the generation of the nanostructured patterns (Supplementary Fig. 5). The FEP electret film was subjected to a corona discharging process to introduce charges, thereby increasing the electrostatic induction (Supplementary Fig. 6a). And then the TENG was constructed through folding two pieces of strip electrodes, as illustrated in Fig. 2f. The charge circulation of this TENG during a compress-release cycle was shown in Supplementary Fig. 6b. The conductive electrode and electret were staggered and stacked with each other in the initial state (State I). When the TENG was moved under the compressive forces, the implant charges into the electret though corona discharging played a key role in charge circulation and leaded to electrostatic induction (State II). And then the triboelectrification effect occurred when the multilayered plates were in close contact with each other (State III). After the removal of the external force, the TENG returned to its original position, and the charges finally flowed back to their initial state (State IV).

Thanks to the double-helix spring origami architecture, this TENG was capable of restoring to its original state from the compressed or stretched state without any auxiliary, showing remarkable elasticity and stretchability (Fig. 2g). In consequence, it could be utilized as energy harvester to convert biomechanical energy of human movements (e.g. finger tapping, elbow bending, and foot tapping) into electricity to power ACEL device. The TENG, for instance, can be integrated into the footwear to availably harness human mechanical energy and provide high convenience for patients (Fig. 2h). The TENG embedded in shoes can be mechanically stimulated periodically when walking or running, facilitating the conversion of compression or stretching forces into AC power to drive the ACEL device (Supplementary Figs. 7 and 8).

## Mechanical and electrical performance of the TENG

The mechanical and electrical performances of the TENG were investigated as a bioenergy harvesting device. The deformations of this TENG were recorded in its compressive and stretched state (Supplementary Fig. 9). Meanwhile, the relationship between force and displacement of the TENG was recorded. As shown in Fig. 3a, the initial length of the TENG without external force was 40 mm, and the maximum tensile and compressive displacement of the TENG were 92 mm and 30 mm, respectively. A linear

compression (purple area) was revealed when the compression strain was less than 56.2% (Fig. 3a, b). And the corresponding Young's modulus in linear compression region was about 6600 Pa, indicating excellent elasticity of this TENG. In order to investigate the long-term elastic performance of this TENG, we conducted compression-rebound experiments with different cycles (10k, 50k, 10k, 150k, and 200k). As depicted in Supplementary Fig. 10, after undergoing 10k, 50k, 100k, 150k, and 200k compressive cycles of this TENG, the corresponding Young's modulus exhibited a reduction of 5%, 9%, 12%, 20%, and 21% respectively compared to the initial value. The Young's modulus exhibited non-obvious alteration when the number of cycles exceeded 150k, indicating the long-term elastic stability for wearable application. Furthermore, once the tensile strain surpassed 230%, this TENG experienced a fracture and consequently lost its functionality (Fig. 3c).

Subsequently, the electrical properties of TENG with a load resistance of 5 MΩ were characterized. As shown in Supplementary Fig. 11a, with the incremental increase in excitation acceleration (1.0 g, 1.5 g, 2.0 g, 2.5 g, and 3.0 g), the output voltage exhibited a significant enhancement from 25 V to 120 V while maintaining a fixed frequency of 15 Hz. And its maximum output voltage demonstrated a positive correlation with the excitation acceleration, while exhibiting a sensitivity of 8 V/(m s$^{-2}$) (Supplementary Fig. 11b). Besides, under the fixed acceleration of 2.0 g, the maximum output voltage of the TENG exhibited a decrease as the frequency increased from 10 Hz to 20 Hz (Supplementary Fig. 11c). Therefore, the output voltage showed a negative correlation with the excitation frequency, demonstrating a slope of -3.44 V/Hz (Supplementary Fig. 11d). While maintaining a fixed peak-to-peak displacement of 2.5 mm, the output voltage significantly increased from 20 V to 160 V with the increased frequency (10 Hz, 12 Hz, 14 Hz, 16 Hz, and 18 Hz) (Supplementary Fig. 11e), indicating a positive correlation relationship with a slope of 10.2 V/Hz (Supplementary Fig. 11f).

This TENG achieved a peak-to-peak open-circuit output voltage of up to 1100 V and exhibited a short-circuit current 100 μA when subjected to foot pressure, indicating its outstanding output performance, as depicted in Fig. 3d–f. And the TENG showed exceptional sensitivity to mechanical stimuli of footsteps with a rapid response time of less than 0.4 s (Fig. 3e). With a load resistance of 5 MΩ, the TENG generated an instantaneous maximum output power of 14.05 mW (Fig. 3g). This TENG has a small surface area of 9 cm$^2$, thus allowing for easy application of forces from human to its cross-sectional area. And its peak-to-peak open-circuit output voltage achieved a negligible change under the force with different applied area (Supplementary Fig. 12). Furthermore, the charge stability of this TENG was investigated through monitoring the surface potential of FEP electret over a period of 30 days (Fig. 3h). The surface potential initially experienced a rapid decline within the first 5 days, followed by stabilization at approximately 55% of its initial value after 30 days. Besides, even after 200,000 contact-release cycles, the output voltage of TENG still exhibited sustained long-term stability (Fig. 3i). Therefore, the continuous output energy of this TENG presents an attractive option for wearable ACEL mPDT device.

## Optical performance of the ACEL mPDT device

For attaining desirable optical ACEL characteristics of the self-powered mPDT device, we further regulated the composition and thickness of PDMS/ZnS:Cu,Al emissive layer. The ACEL intensity was distinctly observed to increase as the weight ratio of ZnS:Cu,Al phosphor increased from 1:1, 1:2, 1:3 to 1:4. Among them, the ACEL device with a 1:4 ratio exhibited the highest emission intensity due to its high distribution density of ZnS:Cu,Al phosphors (Fig. 4a). Moreover, the ACEL intensity significantly increased as the thickness decreased (from 130, 110, 90 to 70 μm), demonstrating that a thinner emitting layer resulted in higher luminance of emitting fluorescence (Fig. 4b). The significant increase in electroluminescence can be attributed to the enhanced electric field strength accompanied with the reduction in film thickness of the emissive layer. Consequently, the optimal emissive layer (PDMS/ZnS:Cu,Al = 1:4, 70 μm) was selected for further investigation.
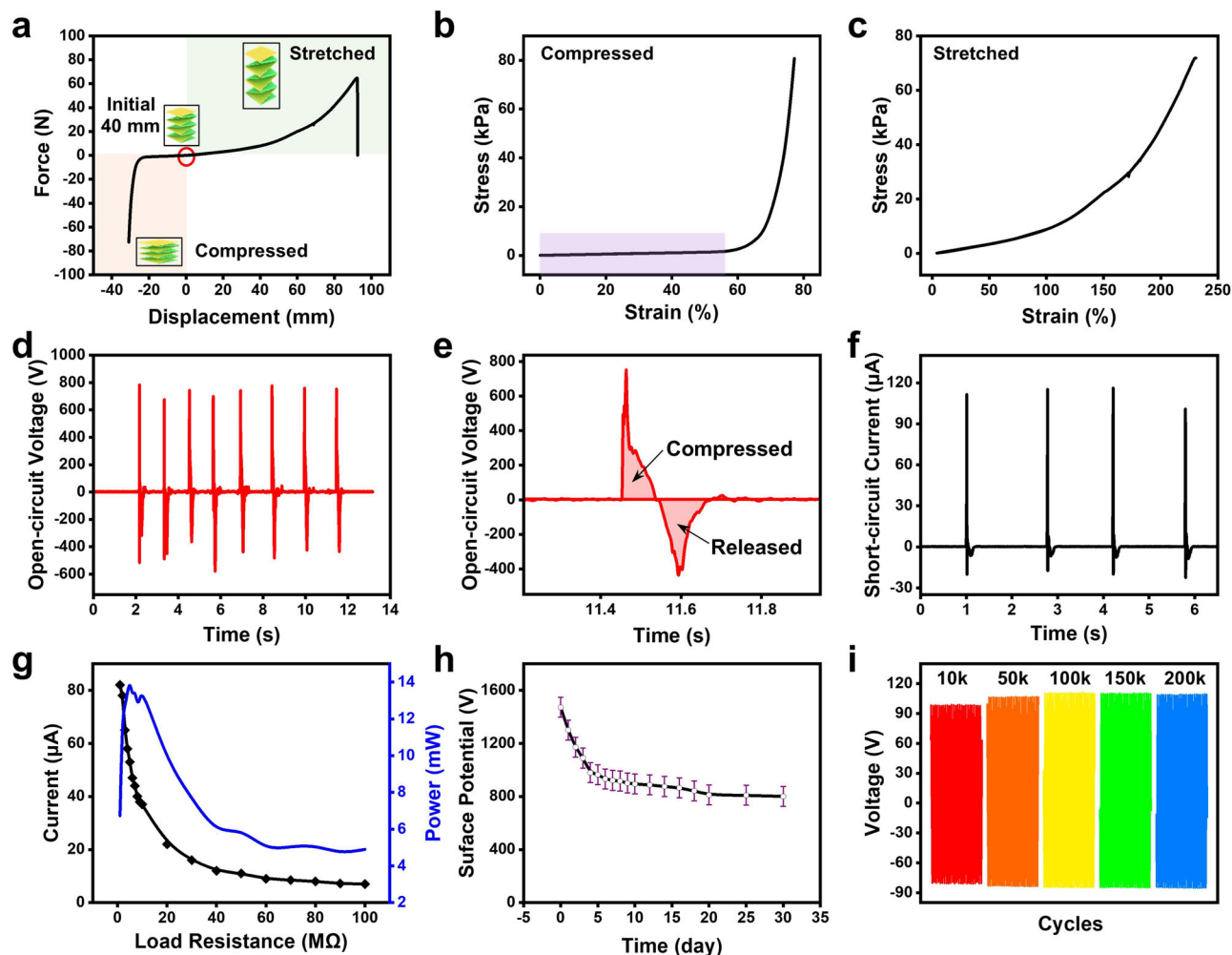
**Fig. 3 | Mechanical and electrical performance of the TENG. a** Force-displacement curve. **b** Compression stress-strain curve. **c** Tensile stress-strain curve. **d** Open-circuit voltage. **e** Open-circuit voltage in one cycle. **f** Short-circuit current. **g** Current and power of the TENG with different load resistances. **h** Stability of the surface potential on FEP over a 30-day period. **i** Output stability of the TENG during cycles.

The uniformity and durability of the optical performance were further investigated using a luminance meter. The ACEL mPDT device exhibited an emission brightness of about 30.62 cd m$^{-2}$, with its luminous area divided into five parts. As a representative surface light source, the ACEL mPDT device showed remarkable uniformity in its luminous properties (Fig. 4c and Supplementary Fig. 13). Moreover, owing to the exceptional flexibility of both the emissive layer and electrode layer, minimal variations in relative ACEL intensity were observed at different bending angles (0°, 30°, 90°, and 150°), as depicted in Fig. 4d. After undergoing 3000 cycles, our device displayed a relative ACEL intensity attenuation of approximately 3.5% (Fig. 4e), showcasing its exceptional long-term stability and repeatability.

The AC electric field generated by TENG, through periodically mechanical stimuli, successfully induced electroluminescence production from this ACEL device within a wavelength range of 450-590 nm (Fig. 4f and Supplementary Video 1). The TENG-driven ACEL device based on emission spectra exhibited that correspond to Commission Internationale de L'Eclairage (CIE) coordinates within the green-light region (Fig. 4g). The xanthene dye RB, which is commonly used in clinical settings, was selected as the PS due to its absorption range of 460–580 nm, ensuring optimal compatibility with the emission spectrum of this ACEL mPDT device. Owing to its exceptional biocompatibility and wide availability, RB has been approved as ophthalmic diagnostic agent and orphan drug for treatment of certain cancers[47]. In addition, the high $^1O_2$ generation efficiency of RB is particularly suitable for ACEL irradiation with low intensity.

## ROS generation of the ACEL mPDT device

In order to validate the successful excitation of RB-loaded hydrogel (RB gel) electrode by ACEL irradiation, the ROS generation potency was detected by the electron spin resonance (ESR). As a type II photosensitizer, RB normally generates $^1O_2$ under light[48]. The presence of $^1O_2$ was investigated utilizing 2,2,6,6-tetramethylpiperidine (TEMP) as a scavenger. Pleasurably, an obvious $^1O_2$-induced signal was detected after 10 min ACEL irradiation of the RB-loaded hydrogel electrode, which became even stronger for the next 20 min, indicating the efficient $^1O_2$ production of the ACEL mPDT device (Fig. 4h). In contrast, the hydrogel electrode without PS showed unaltered intensity of $^1O_2$ characteristic signal when subjected to ACEL irradiation for either 10 or 20 minutes (Supplementary Fig. 14a). As shown in Supplementary Fig. 14b, the absorbance of 1,3-diphenylisobenzofuran (DPBF) exhibited a gradual decrease with an increase in light intensity (from 30, 50, 100 to 150 cd m$^{-2}$) during 20 min irradiation, indicating accelerated degradation of DPBF under higher brightness. These results demonstrated that an increase in the production of ROS increased with the enhancement in emission brightness during the same irradiation time. In addition, under the reduced-dose irradiation of the ACEL device (30 cd m$^{-2}$), ROS can continuously generate over time, as depicted in Supplementary Fig. 14c.

Furthermore, the therapeutic mechanism of this ACEL mPDT device was explored. Previous studies have indicated that thin Cu$_x$S needles are embedded in the ZnS lattice to profitably form the Schottky barrier[49]. The injection of electrons and holes from the opposite ends of Cu$_x$S needles to the ZnS lattice occurs through tunneling under a high local electric field.
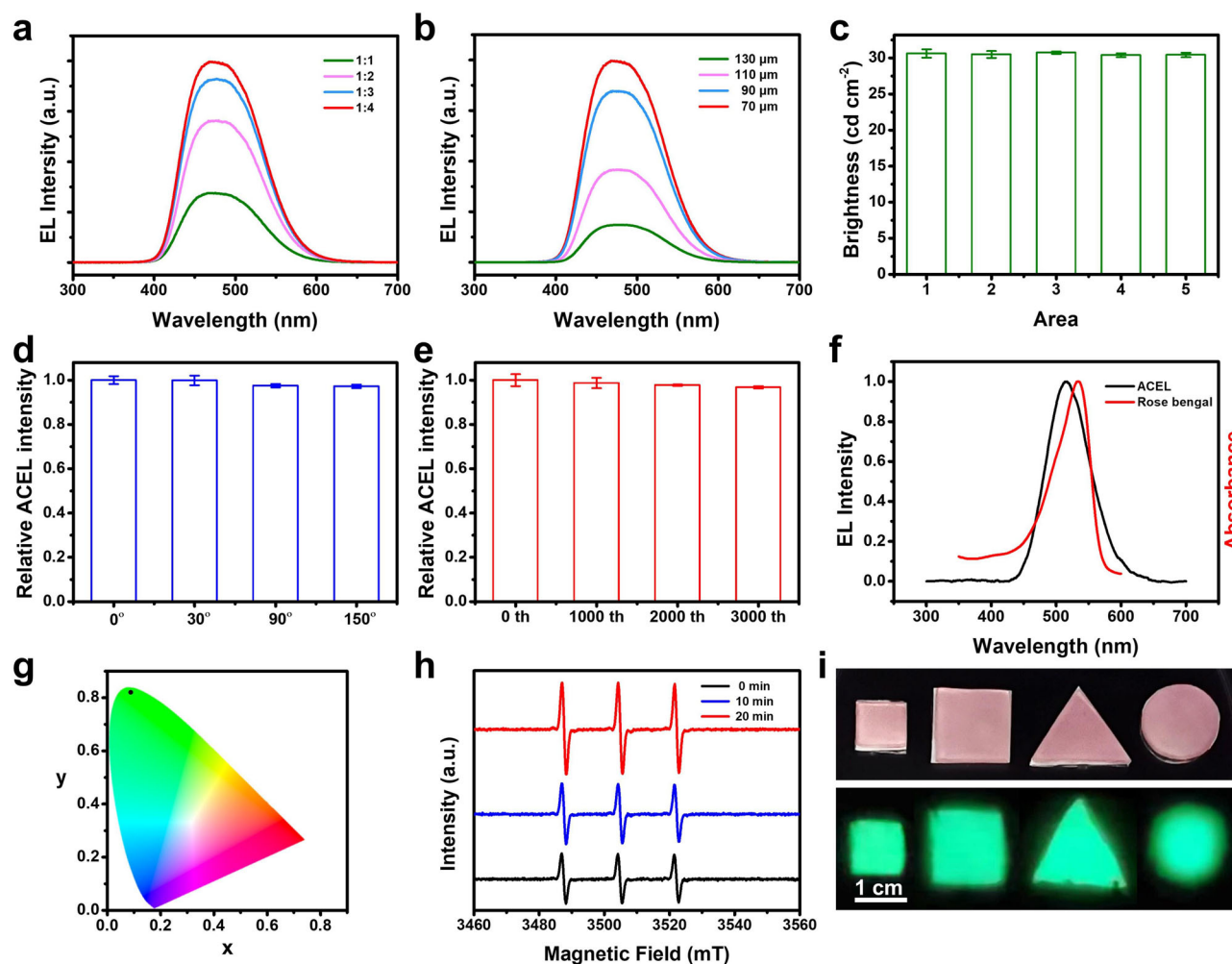
**Fig. 4 | Characterization of the ACEL mPDT device.** The electroluminescence intensity of this ACEL mPDT device at **a** different weight ration of PDMS/(ZnS:Cu,Al) and **b** various thickness of emissive layer. **c** The emission brightness of the ACEL device' different area. (*n* = 3). Error bars: standard deviation. This ACEL device is divided into five areas, and its emission brightness is recorded using a luminance meter. Relative ACEL intensity of the ACEL mPDT device at **d** various bending angles and **e** bending cycles. (*n* = 3). Error bars: standard deviation. **f** The electroluminescence spectrum and RB absorbance spectrum. **g** Commission Internationale de L'Eclairage (CIE) coordinates of the ACEL mPDT device. **h** ESR spectra of $^1O_2$ generated by ACEL mPDT device. **i** The electroluminescent photographs of the ACEL mPDT device with different sizes and shapes.

Subsequently, these charge carriers become trapped at luminescent centers located at donor sites (Al) and acceptor sites (Cu), leading to recombination and accompanied electroluminescence emission[49]. Meanwhile, the ACEL emitted from the emissive layer was efficiently absorbed by the close-contacted RB hydrogel electrode layer. Next, the RB molecules migrate from ground state to a short-lived single excited state and then to a long-lived triple state through intersystem crossing. Finally, the triple-excited RB molecules undergo a reaction with the surrounding molecular oxygen to generate $^1O_2$ (Fig. 1b). Therefore, this ACEL device with remarkable ROS generation ability holds immense potential as a dynamic therapeutic platform.

## Tailorability of the ACEL mPDT device

The shapes, sizes, and locations of skin wounds normally display variations. The existing wearable PDT devices with rigid and small-sized light sources are unsuitable for treating the irregular and large-sized lesions. For instance, the construction of LED arrays is imperative to ensure the adequate lesion coverage owing to the limited light beam area of LED point source. Despite its potential for large-scale integration, OLED is particularly sensitive to dimensional variations accompanied by the generations of leakage current[33]. Due to its arbitrary tailorability and dimensional variations' conformability, our ACEL mPDT device offered effortless customization into various shapes

and sizes, such as squares, circles, and triangles (Fig. 4i). Besides, the ACEL mPDT devices, regardless of their diverse shapes, still maintained consistent green fluorescence (Supplementary Video 2). Meanwhile, the ACEL device demonstrated full flexibility, enabling it to achieve conformal contact with pathological tissues or organs of irregular area and shapes. Therefore, the customizable ACEL device facilitates on-demand mPDT in clinical setting and personalized health management.

## In vitro antimicrobial therapeutic efficacy

Encouraged by the effective ROS generation of the ACEL mPDT device, its antimicrobial efficacy was evaluated towards a broad spectrum of micro-organisms, including drug-resistant Gram-positive bacteria methicillin-resistant *Staphylococcus aureus* (MRSA), oxacillin-resistant *S. aureus* USA-300 (USA-300), *S. aureus* BAA-40 (BAA-40), and vancomycin-resistant *Enterococci* (VRE), drug-resistant Gram-negative bacteria tetracycline-resistant *Escherichia coli* (TRE), and pathogenic fungi *Candida albicans* (*C. albicans*). These pathogens were treated by the ACEL mPDT device at a concentration of ~$10^5$ colony forming unit (CFU) cm$^{-2}$.

After the ACEL-induced mPDT for 1 h, the antimicrobial performance was evaluated using CFU counting. As shown in Fig. 5a, the ACEL mPDT device exhibited powerful antibacterial effect against MRSA, and the corresponding number of viable bacteria was reduced by
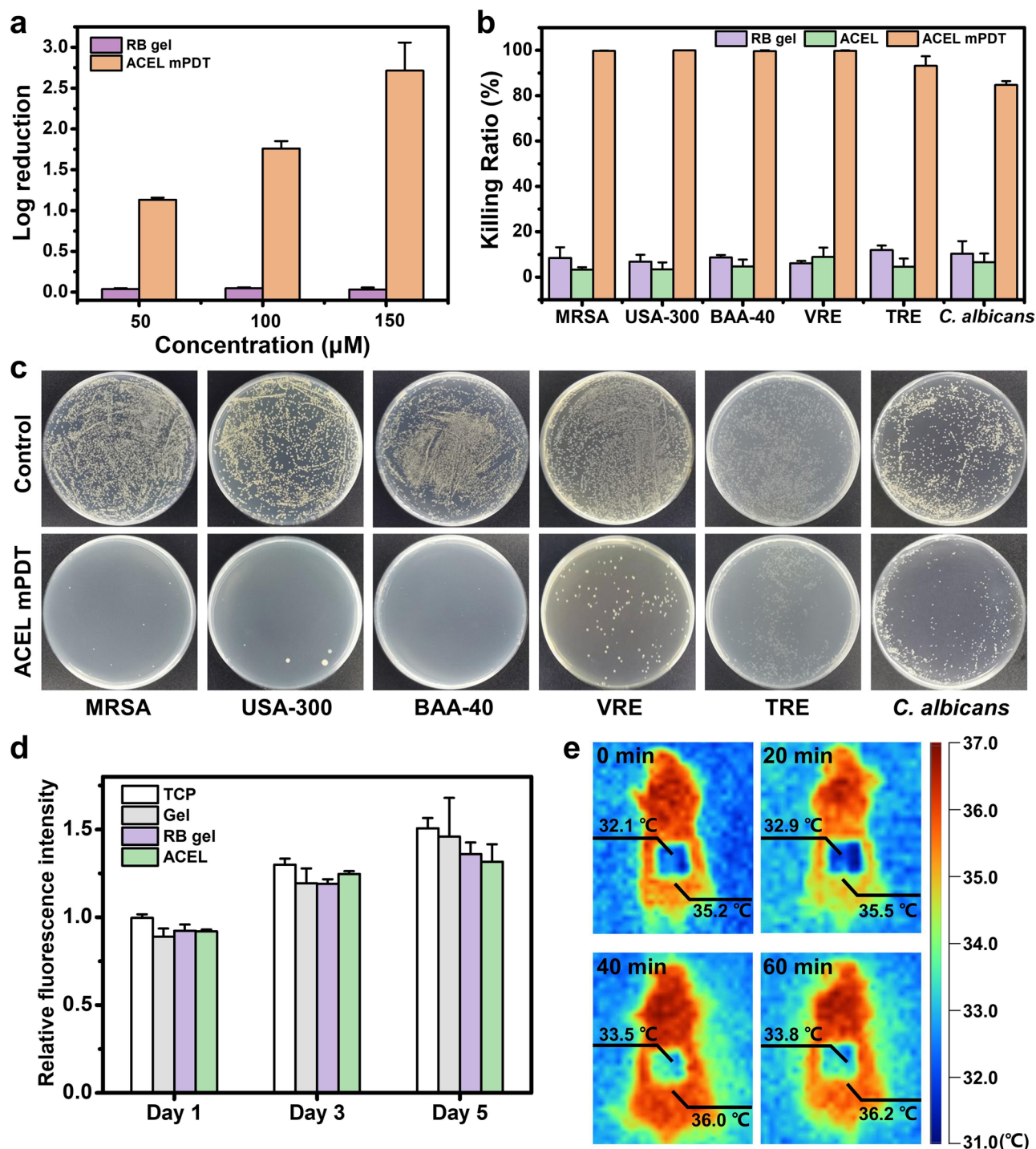
**Fig. 5 | In Vitro antimicrobial activities and biocompatibility.** Killing ratio of **a** MRSA treated by ACEL mPDT device with different RB concentrations (50 μM, 100 μM, and 150 μM) and **b** Gram-positive bacteria (MRSA, USA-300, BAA-4, and VRE), Gram-negative bacteria (TRE), and fungi (*C. albicans*) treated with PBS, RB gel, ACEL, and ACEL mPDT. (*n* = 3) Error bars: standard deviation. **c** Photographs of the colonies of MRSA, USA-300, BAA-40, VRE, TRE, and *C. albicans* treated with different groups. The bacterial suspensions are spread on the LB agar plates and then incubated at 37 °C for 12 h. And the bacterial colonies are recorded using a camera. **d** Cell viabilities of NIH3T3 cells treated with TCP, gel, RB gel, and ACEL. (*n* = 3) Error bars: standard deviation. **e** IR thermal images of mice treated with ACEL mPDT device.

1.13 ± 0.03, 1.76 ± 0.09, and 2.71 ± 0.3 orders of magnitude respectively with the photosensitizer concentration from 50, 100 to 150 μM. Therefore, the hydrogel electrode with PS concentration at 150 μM was chosen for further eradication of drug-resistant bacteria. As shown in Fig. 5b, without ACEL irradiation, the RB gel exhibited negligible antibacterial effect. Besides, the ACEL irradiation alone caused little damage to pathogenic bacteria. In sharp contrast, the ACEL mPDT device achieved more than 99% killing efficacies towards Gram-positive bacteria, including MRSA, USA-300, BAA-40, and VRE. In addition, the inhibition rate for TRE and *C. albicans* achieved to > 93% and > 84%, respectively. Corresponding trend could be clearly observed in the plate of colonies (Fig. 5c and Supplementary Fig. 15). All these results collectively demonstrated that such ACEL mPDT device exhibited effective bactericidal activities in vitro.

The antibacterial mechanism of ACEL mPDT was investigated using SEM. As presented in Supplementary Fig. 16, all bacterial cells exhibited intact and smooth cell membranes in the control group. Similarly, in the absence of ACEL irradiation, the bacteria in contact with RB gel were also observed to have comparable intact morphology. Besides, even after ACEL irradiation for 1 h, the bacterial morphology remained largely unchanged in the absence of PS. Prominently, after treatment with ACEL mPDT device, the cell membranes of these microorganisms exhibited prominent collapse or shrinkage, accompanied by the presence of visible perforations (indicated by white arrows), thus demonstrating significant bacterial damage. The powerful impact of $^1O_2$ generated by our ACEL mPDT device is primarily responsible for this phenomenon. As a major species in PDT[50,51], $^1O_2$ can cause extreme oxidative damage on the bacterial cell membranes, leading to leakage of intracellular matrix and inducing apoptosis[52]. Notably, the ACEL mPDT device mainly attacks biomolecules without requiring specific bacterial targets, thereby preventing the development of drug resistance and offering a prospective tool against drug-resistant bacteria.

### In vitro and in vivo biocompatibility

The biocompatibility of wearable therapeutic device is a prerequisite especially for a long-period utilization. Thus, the in vitro hemolysis and cytotoxicity of our ACEL mPDT device were firstly investigated. The intactness of mammalian red blood cells was demonstrated in Supplementary Fig. 17. No significant hemoglobin release was observed after incubation with our prepared hydrogels. The hemolysis ratio remained below the permissible level of 5.0% even after ACEL irradiation for 1 h, indicating the excellent hemocompatibility of this device. Moreover, the in vitro cytotoxicity was further evaluated by co-culturing with mammalian fibroblast cells NIH3T3 for a duration of 5 days, and the viability of the cells was determined using the alamarBlue assay. The fibroblast cells exhibited continuous growth throughout the testing period, as depicted in Fig. 5d. Notably, their viability not showed significant difference compared to the control tissue culture plate (TCP) group at 1, 3, and 5 days ($p > 0.05$). Besides, the LIVE/DEAD staining results proved that NIH3T3 cells co-cultured with gel, RB gel, and ACEL showed robust green fluorescence and maintained their characteristic spindle-shaped appearance, indicating their healthy state (Supplementary Fig. 18). These results clearly demonstrated that our ACEL mPDT device exhibited negligible cytotoxicity towards NIH3T3 cells and did not impede their proliferation. Therefore, the in vitro biocompatibility of the ACEL mPDT device ensures its long-period biosafety for in vivo therapeutic applications.

The infrared thermal imaging and histological analysis were further performed to assess the in vivo biosafety of the ACEL mPDT device during its usage. The conventional physical light sources commonly used in PDT typically require high levels of irradiation intensity, which can potentially pose a thermal hazard to the skin tissues. Thus, wearable PDT devices must minimize their photothermal generation to ensure patient safety. The temperature of mice's skin treated with the ACEL mPDT device was observed using infrared thermal imaging. As shown in Fig. 5e, the temperatures of both the ACEL mPDT device and the surrounding skin remain relatively stable after 60 min of continuous ACEL irradiation, indicating insignificant thermal effects compared to their initial states. Therefore, as a non-thermal light source, the ACEL device offers dependable safety for long-term wearable mPDT applications. Moreover, the potential toxicity induced by wearing the ACEL mPDT device was further investigated by the histological analysis of major organs, including heart, liver, spleen, lung, and kidney[53]. After a two-week period of wearing, the tissues were sectioned and evaluated through the hematoxylin and eosin (H&E) staining. Compared to the normal tissues, no significant inflammation or damage was observed after continuous wearing of the ACEL mPDT device, indicating its non-toxicity (Supplementary Fig. 19).

### ACEL mPDT device for an infected model in vivo

The self-powered ACEL device eliminates the need for inconvenient external light and power sources, and offers a wearable and user-friendly mPDT model. The aforementioned studies have proved that the ACEL mPDT device has potent efficacy in eradicating drug-resistant bacteria in vitro, as well as excellent biocompatibility both in vitro and in vivo. The antibacterial performance of the ACEL mPDT device was further verified in vivo. A full-thickness skin wound with 8 mm diameter was created on the back of Kunming mice and inoculated with $10^5$ CFU MRSA to establish a localized infection model. Subsequently, the ACEL mPDT device was applied to the dorsal region of the mice using a linear motor driving at 1 Hz for 1 h every other day to treat infected wound, while PBS-treated wound was used as the control group (Fig. 6a, b, Supplementary Fig. 20, and Supplementary Video 3).

The photographs of the MRSA-infected wounds with different treatments were recorded and shown in Supplementary Fig. 21. The wounds treated with PBS, RB gel, and ACEL irradiation exhibited obvious suppurative phenomena, indicating a severe bacterial infection state. However, after being treated with the ACEL mPDT device, the wounds presented a cleaner environment, revealing its potent antibacterial efficacy in vivo. The quantitative statistics of wound closure rates indicated that a significantly accelerated healing process in mice treated with the ACEL mPDT device compared to other treatments (Fig. 6c). In addition, the survival bacteria numbers in the wound tissues were evaluated. Abundant viable MRSA colonies ($2.7 \sim 2.9 \times 10^5$ CFU $g^{-1}$) existed in the PBS, RB gel, and ACEL irradiation treated wounds, indicating successful establishment of bacterial infection. In contrast, the survival bacteria in ACEL mPDT treated wound tissues exhibited a sharp decrease of 88% ($3.4 \times 10^4$ CFU $g^{-1}$), clearly demonstrating the efficacy of this ACEL mPDT device in inhibiting bacterial infections in vivo (Fig. 6d, e).

Furthermore, on the 8th day post-treatments, the surrounding tissues of the wound were sectioned and assessed using H&E and Masson staining (Fig. 6f). Traditionally, neutrophils as the primary immune cells will be recruited to an inflamed tissue[54]. H&E staining revealed a significant extravasation of neutrophil cells (depicted as purple spots) in the wound tissues of the PBS, RB gel, and ACEL irradiation treatment groups, indicating a serious inflammation state caused by bacterial infection. Comparatively, in the ACEL mPDT treated group, a significant reduction in neutrophils was observed, which can be attributed to its potent efficacy in inhibiting bacterial infection thus suppressed the inflammatory responses. In addition, the collagen deposition and organization in healing process of new skin tissues were evaluated through Masson's trichrome staining. More densely packed mature collagen fibers were observed in the ACEL mPDT treated tissues compared with PBS, RB gel, and ACEL irradiation treatments. This phenomenon suggested the ACEL mPDT potentially promoted wound tissue regeneration during the healing process. Above histopathological results collectively demonstrated that the ACEL mPDT device can effectively suppress inflammatory response by eradicating bacterial infection, thereby exhibiting improved tissue regeneration for expediting full-thickness infected wound healing in vivo.

### MRSA-infected diabetic wound healing in vivo

Diabetic wound as a representative type of chronic wound is highly susceptible to bacterial invasion[55]. The management of infected diabetic wounds has emerged as a formidable challenge in clinical practice[56]. We constructed a drug-resistant bacteria-infected chronic wound model on the streptozotocin-induced diabetic C57BL/6 mice. The wounds on the back were treated with the daily administration of PBS, RB gel, ACEL irradiation, antibiotic, and ACEL mPDT for 7 days (Fig. 7a). High level MRSA burden ($5.4–7.2 \times 10^7$ CFU $g^{-1}$) were observed in the wound tissues treated with PBS, RB gel, and ACEL irradiation due to the rapid proliferation of bacteria in diabetic wounds with impaired immune system in mice. In addition, the antibiotic treatment of methicillin was also undefendable to the attack of drug-resistant bacteria. However, the application of ACEL mPDT for 1 h per day, resulted in a remarkable bacterial count reduction of 2 orders of magnitude, demonstrating its potent antibacterial efficacy (> 99%) in this MRSA-infected diabetic wounds (Fig. 7b and Supplementary Fig. 22).
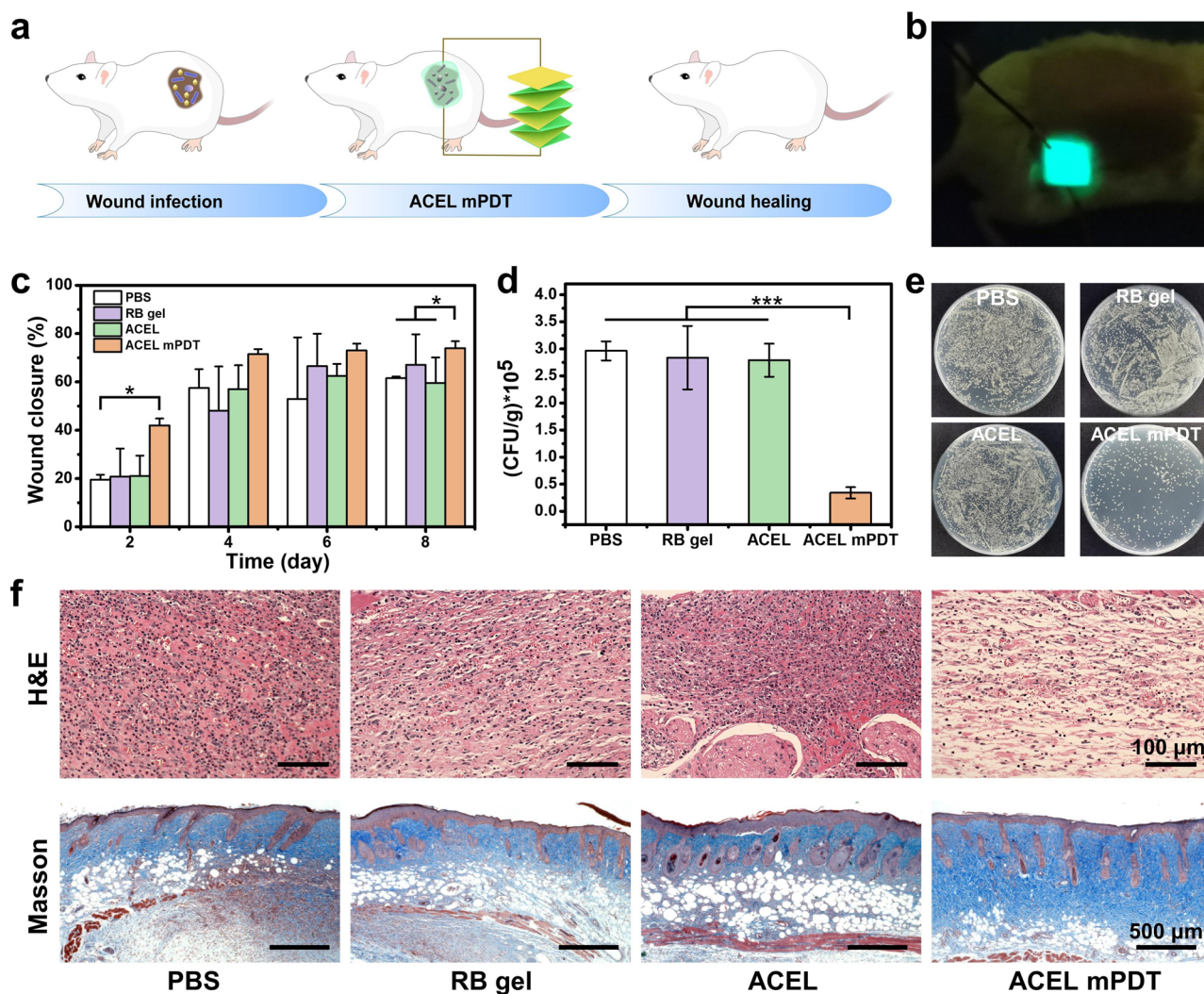
**Fig. 6 | Infected full-thickness skin wound model. a** MRSA-infected wound model. A full-thickness MRSA-infected wounds (8 mm in diameter) are created on the back of the mice. Then, this designed TENG-driven ACEL mPDT device is applied on the infected wound for treatments. **b** Photograph of the ACEL mPDT device worn on the back of the mice. Under the driving of TENG, this ACEL mPDT device emits green electroluminescence. **c** Wound closure rates on different days ($n = 3$). Statistical data between the 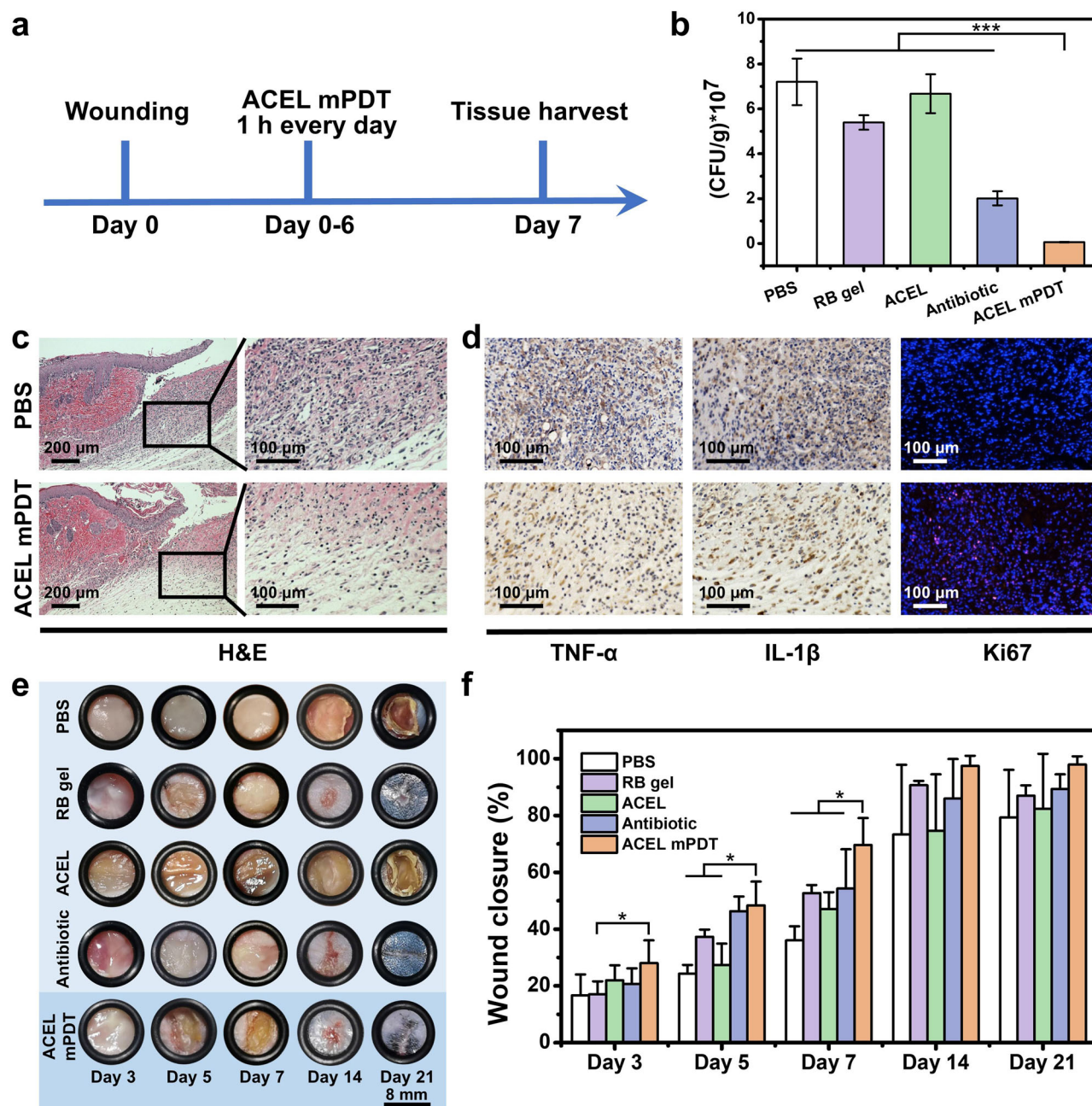corresponding groups are denoted as $*p < 0.05$, $**p < 0.01$, $***p < 0.001$. Error bars: standard deviation. **d** Colony numbers of MRSA obtained from the wounds ($n = 3$). Statistical data between the corresponding groups are denoted as $*p < 0.05$, $**p < 0.01$, $***p < 0.001$. Error bars: standard deviation. **e** Photographs of MRSA colonies obtained from the wounds treated with PBS, RB gel, ACEL, and ACEL mPDT. The bacterial suspensions are spread on the LB agar plates and then incubated at 37 °C for 12 h. And the bacterial colonies are recorded using a camera. **f** H&E and Masson staining of the wound tissues.

Additionally, histopathological, immunohistochemical, and immunofluorescent staining were performed to observe the repair state of infected diabetic wounds on the 7th day. Excessive inflammation, insufficient angiogenesis, and reduced cell proliferation are the major causes for the delayed healing of diabetic wounds[57]. Abundant neutrophil infiltrations were detected in the tissues treated with PBS, RB gel, ACEL irradiation, and antibiotic that due to the intense inflammation response caused by MRSA infection. In sharp contrast, a significant decrease of neutrophils was observed in tissue treated with ACEL mPDT, indicating an alleviated inflammatory state (Fig. 7c and Supplementary Fig. 23). For the immunohistochemical staining, the expression levels of proinflammatory cytokines TNF-$\alpha$ and IL-1$\beta$ in the ACEL mPDT treated diabetic wound tissue were also apparently decreased compared to the PBS control group (Fig. 7d). These results indicated the chronic wound inflammation could be significantly controlled through the effective bacterial infection inhibition of ACEL mPDT. Furthermore, the immunofluorescence staining of Ki67, a cell proliferation marker, was also performed to evaluate the proliferative activity of the diabetic wound tissue during healing process[58]. Compared with the PBS-treated tissue, the ACEL mPDT group exhibited a higher expression of Ki67 that indicated the cells of wound tissue in a more rapid and effective proliferative state (Fig. 7d).

Subsequently, the wound healing process with different treatments was evaluated for 21 days (Fig. 7e, f). In the first 7 days, typical yellow exudates were obviously observed in the wounds of the PBS, RB gel, ACEL irradiation, and antibiotic treated groups, indicating the acute infection caused by MRSA inoculation. In contrast, the ACEL mPDT device treated wound maintained a clean environment without noticeable exudates that benefited from the efficient inhibition of bacterial infection. The wound closure rate of ACEL mPDT treated groups (97%) is apparently faster than the other groups (73–90%) at the 14th day. This accelerated healing phenomenon may be attributed to the ROS functions in the potent antibacterial effect, and stimulation of angiogenesis[59]. On the 21th day, the wound treated with ACEL mPDT almost fully closed. However, the wounds in other groups were still fell behind it, which mainly due to the bacterial infection-induced prolonged inflammation and impaired cell migration and proliferation[60]. These results revealed that our designed ACEL mPDT device could efficiently eradicate drug-resistant bacteria infection and accelerate the healing of chronic wound in vivo.

**Fig. 7 | MRSA-infected diabetic chronic wound model. a** Establishment of an infected diabetic wound model and its treatment process. **b** Colony numbers of MRSA obtained from the wounds (*n* = 3). Statistical data between the corresponding groups are denoted as \*$p < 0.05$, \*\*$p < 0.01$, \*\*\*$p < 0.001$. Error bars: standard deviation. **c** H&E staining of the wound tissues. **d** Immunohistochemistry staining of TNF-α and IL-1β and Ki-67 staining in different groups. **e** Representative photographs of the infected wounds with different treatments at varied time points. A full-thickness MRSA-infected wound (8 mm in diameter) is created on the back of a diabetic mice, and a black ring as a dimensional reference substance is placed on the wounds (diameter of the black ring: 8 mm). Changes in infected wound dimensions are recorded using a camera. **f** Wound closure rates of five groups on different days. (*n* = 3). Statistical data between the corresponding groups are denoted as \*$p < 0.05$, \*\*$p < 0.01$, \*\*\*$p < 0.001$. Error bars: standard deviation.

## Discussion

Here, we presented a proof-of-concept wearable self-powered ACEL mPDT device, in which the human motion-driven metronomic ACEL activates the PS-loaded hydrogel electrode to generate ROS in situ for prolonged management of chronic wounds. Comparing with the conventional phototherapy equipment, this flexible and integrated ACEL mPDT device could be customized to arbitrary shape and size, and still maintain consistent electroluminescence, making it suitable for irregular lesion wounds and human-sized form factor. The self-powered therapeutic device can overcome the restrictions of batteries such as limited lifespan and potential safety hazards. Besides, this body-worn optoelectronic device showed remarkable antibacterial efficacy against both drug-resistant bacteria and pathogenic fungi in vitro, as well as potent inhibition of infection and inflammation to accelerate healing of a MRSA-infected diabetic wound in vivo. In addition, it also exhibited reliable biosafety and negligible photothermal generation without causing tissue damage, and thus is well appropriate for long-term wearable mPDT.

This ACEL mPDT device dexterously breaks the limitations of conventional PDT with bulky and rigid optical instruments, uncomfortable transvenous administration, and specialized professionals, offering a

promising option for next-generation personal PDT device. Notably, it not only effectively combats the wound infections, but also exhibits the potential to treat other kinds of superficial lesions. Furthermore, with the assistance of light transmission techniques such as optical fiber, this ACEL device is also anticipated for deep tissue lesion treatments in the future. To expand the applications of ACEL mPDT, the energy supply strategy with different modes will be further implemented such as the combination of batteries with AC output and bioenergy harvester. Our designed ACEL mPDT device, therefore, provides a therapeutic platform with potent effectiveness, on-demand customization, and unrestrained manoeuvrability, pushing the development of wearable optoelectronic medical devices in the out-of-hospital settings.

## Methods

### Materials

Potassium persulfate (KPS) (purity > 99.5%), *N,N'*-methylenebisacrylamide (MBA) (purity > 99.0%), NaCl (purity > 99.5%), and rose bengal (RB) (purity > 90.0%) were purchased from Adamas-beta (China). Acrylamide monomer (AM) (purity > 98.0%) was ordered from Tokyo Chemical Industry. Polydimethylsiloxane (PDMS) was purchased from Dow Corning. ZnS:Cu,Al microparticles were purchased from Shanghai KPT company. The fluorinated ethylene propylene (FEP) electret films were obtained from Goodfellow (Shanghai) Trading Co., Ltd. The stripe electrodes were ordered from Xi'an Beilin district Jingxinfu electronic business company. Streptozotocin (STZ) was purchased from Shanghai yuanye Bio-Technology Co., Ltd. AlamarBlue assay kit and LIVE/DEAD BacLight kit were obtained from Thermo Fisher Scientific (USA). Methicillin-resistant *Staphylococcus aureus* (MRSA), *S. aureus* BAA-40, oxacillin-resistant *S. aureus* USA-300, vancomycin-resistant *Enterococcus* (VRE), tetracycline-resistant *Escherichia coli* (TRE, ER2738), *Candida albicans* (*C. albicans*, ATCC 10231), and mouse embryonic fibroblast cells (NIH3T3, ATCC CRL-1658) were procured from American Type Culture Collection.

### Synthesis of hydrogel electrode

Hydrogel electrode of this ACEL mPDT device was synthesized through the free radical polymerization of AM. Briefly, NaCl (2 g) was completely dissolved in the DI water (10 mL) at 70 °C, followed by the dissolution of AM (0.9 g), MBA (0.014 g), and KPS (0.028 g) in the aforementioned solution. Subsequently, this mixed solution was added into a customized mold to further free radical polymerization at 55 °C for 4 h.

### Synthesis of PS-loaded hydrogel electrode

Similar to the preparation process of above hydrogel electrode, a PS-loaded hydrogel electrode was prepared as followed: the photosensitizer RB was added into the solution containing with NaCl and AM. Then, MBA and KPS with same concentration were added to the mixed solution to construct RB hydrogel electrode as a therapeutic patch.

### Synthesis of emissive layer

Firstly, the component A of PDMS was mixed with ZnS:Cu,Al phosphor microparticles and adequately stirred for 1 h. Subsequently, the component B of PDMS (prepolymer : cross-linker = 10 : 1) was added into above solution, and then continue to mix well. Above solution was coated on the surfaces of glass to form flexible film using an adjustable film applicator. Finally, the emissive layer was heated for 6 h at 80 °C to cure, and stripped from the surfaces of glass.

### Device characterization

The cross section of the emissive layer was observed using SEM (FEI Verios G4). The ACEL spectra were measured using an ocean optics spectrometer (QE65 Pro). The brightness of ACEL mPDT device were measured through a luminance meter (LS-150). The electrical performances of the TENG were characterized using an electrometer system (Keithley 6514). The mechanical performance of the TENG were tested through a universal testing machine (KY-500NW). The IR thermal images of mice treated with ACEL mPDT device were detected by infrared camera (Fluke TiS10).

### Detection of reactive oxygen species

The production of ROS in the ACEL mPDT device was characterized by the electron spin resonance (ESR) technique. The hydrogels were cut into tablets (1 cm×1 cm×0.1 cm) and then placed in a quartz cell containing 1 mL of PBS with $^1O_2$ trapper 2,2,6,6-tetramethylpiperide (TEMP). Under the ACEL irradiation, the signals of $^1O_2$ were further detected. The absorption spectra of DPBF were tested using Ultraviolet-Visible Spectrophotometer.

### Hemolytic activity test

Fresh rabbit blood was collected through the ear vein, followed by centrifugation to get red blood cells (RBCs). The RBCs subsequently subjected to five washes with tris buffer and ultimately diluted to a concentration of 5% v/v. And the prepared hydrogels were placed at the bottom of 48-well plate. The RBCs solution (200 μL) was added to each well and incubated at 37 °C with 150 rpm shaking for 60 min. Triton X-100 (0.1%) in normal saline (NS, 0.9% NaCl) solution and NS solution were selected as the control positive and negative groups, respectively. The microplate was centrifuged at 1000 rpm for 10 min. Afterwards, 80 μL aliquots of the supernatant were transferred to the wells of a new microplate and diluted with an additional 80 μL of Tris buffer. The absorbance (540 nm) was tested using a microplate reader (Spark, Tecan, Switzerland). The hemolysis value was determined using the Eq. 1:

$$\%\text{hemolysis} = \frac{A(\text{sample}) - A(\text{negative})}{A(\text{triton}) - A(\text{negative})} \times 100\% \qquad (1)$$

### In vitro biocompatibility study

The biocompatibility of the ACEL mPDT device was further assessed. NIH3T3 fibroblast cells were seeded onto a 24-well plate (approximately $1 \times 10^4$ cells per well). After further incubation for 24 h, the round-shaped hydrogels (0.5 cm in diameter) were immersed in DMEM for 2 h and subsequently transferred into a 24-well culture plate co-incubated with NIH3T3 fibroblast cells. The cells were exposed to ACEL irradiated for 1 h daily. The culture mediums were refreshed every 2 days. Cell viability was investigated using alamarBlue assays and LIVE/DEAD assays.

### In vitro antibacterial assays

The ACEL mPDT device was evaluated for its antibacterial ability against the typical Gram-positive bacteria (MRSA, USA-300, BAA-40, VRE), Gram-negative bacteria (TRE), and fungi (*C. albicans*). The bacteria were cultured in the LB medium until reaching the mid-log growth phase, followed by three rinses with PBS. The bacterial suspension (10 μL, $\sim 10^7$ CFU mL$^{-1}$) was coated on the surface of preparative materials. After treatments for 1 h, the hydrogels were placed in a 24-well plate containing of PBS (990 μL) and subjected to 3 min ultrasonic treatment to detach bacteria from the materials surfaces. The bacterial suspensions were subsequently 10-fold diluted to various concentrations and plated on the LB agar plates. Lastly, the plates were incubated t 37 °C for 12 h.

### Bacterial morphology observation

The bacterial morphologies with different treatments were observed using SEM. Initially, the bacterial suspension (10 μL, $\sim 10^7$ CFU mL$^{-1}$) was evenly spread on surfaces of this device. After ACEL irradiation (1 h), the bacteria were further incubated for 1 h and then fixed with 4% glutaraldehyde at 4 °C for 4 h. the subsequent dehydration was performed using graded ethanol solutions (20%, 40%, 60%, 80%, 90%, and 100%) for 20–30 min, respectively. And then the bacteria were imaged using SEM after sputter-coated gold (10 Ma, 120 s).

### In vivo antimicrobial assays

Male Kunming mice and C57BL/6 mice were purchased from the Laboratory Animal Unit of Xi'an Jiaotong University. All animal experiments studies were conducted in accordance with the guidelines of the Administration of Laboratory Animals of China (2017 revision) and approved by the animal ethics committee of Northwestern Polytechnical University.

After depilating the back of the Kunming mice, two full-thickness skin wounds (8 mm in diameter) were surgically created on their backs under anesthesia. Then, 10 μL MRSA suspension ($10^7$ CFU mL$^{-1}$) was added on the wound site for 6 h to establish the infection model. Subsequently, the wounds were randomly treated as follows: (1) PBS, (2) RB gel, (3) ACEL for 1 h, and (4) ACEL mPDT for 1 h. The aforementioned treatments were performed every other day for 7 days. In addition, the healing progress of wounds was documented using a digital camera on 2th, 4th, 6th, and 8th day post-treatments. Simultaneously, the areas and closure rates of wounds treated with different various intervention were measured and calculated using the Eq. 2:

$$\text{Remaining wound area}(\%) = \frac{\text{Wound area at day 0} - \text{Wound area at certain day}}{\text{Wound area at day 0}} \times 100\%$$

(2)

Furthermore, on the 8$^{th}$ day post-treatment, the wound tissues were excised. A part of wound tissues was homogenized in sterile PBS and diluted to various concentrations for CFU analysis. The bacteria solution (50 μL) was evenly sprayed onto an LB agar plate and incubated overnight. In addition, the other part of the wound tissues was fixed in 4% formaldehyde, followed by embedding in paraffin and sectioning at a thickness of 4 mm for Masson's trichrome and Hematoxylin-Eosin (H&E) histological observation.

### In vivo diabetic wound healing evaluation

The 5-week-old male C57BL/6 mice daily were intraperitoneally injected STZ (50 mg kg$^{-1}$) for four days. The blood glucose levels were measured after one week, and mice were defined as diabetic mice as those exhibiting fasting blood glucose levels > 17.6 mmol L$^{-1}$ in two consecutive measurements. Then, the diabetic mice were anesthetized and shaved on their backs. The full-thickness skin wound (8 mm in diameter) were produced on the dorsum of the diabetic mice. And MRSA suspension (10 μL, $10^7$ CFU mL$^{-1}$) was added on the wound site for 6 h to construct the chronic infected model. The mice were then randomly assigned into five groups, followed by various treatments of PBS, RB gel, ACEL, antibiotic methicillin (50 μg mL$^{-1}$), and ACEL mPDT with 1 h per day for 7 days using a linear motor driving at 1 Hz. The wound healing process were recorded through a digital camera on 3, 5, 7, 14, and 21 days after different treatments. Simultaneously, the closure rates of wounds were measured and calculated.

In addition, on the 7th day post-treatments, the wound tissues were cut off. The CFU analysis and histological observation process of C57BL/6 mice were same as Kunming mice. Images of the stained tissues were captured by an inverted fluorescence microscope (Evos FL Auto 2).

### Statistical analysis

All experimental data were taken from distinct samples. All data were expressed as mean ± standard deviation. Significance between the two groups was analyzed using Student's $t$ test by Origin software. $P < 0.05$ was considered statistically significant. *($p < 0.05$), **($p < 0.01$), and ***($p < 0.001$).

### Data availability

The data that support the findings of this study are available from the corresponding author upon reasonable request.

### References

1. Kipshidze, N., Yeo, N. & Kipshidze, N. Photodynamic therapy for COVID-19. *Nat. Photon.* **14**, 651–652 (2020).
2. Xiong, J. et al. Engineering a theranostic platform for synergistic hypoxia-responsive photodynamic therapy and chemotherapy. *Matter* **5**, 1502–1519 (2022).
3. Zhang, J. et al. An electroluminodynamic flexible device for highly efficient eradication of drug-resistant bacteria. *Adv. Mater.* **34**, 2200334 (2022).
4. Yao, Q. et al. The concept and examples of type-III photosensitizers for cancer photodynamic therapy. *Chem* **8**, 197–209 (2022).
5. Li, F. et al. Responsive assembly of upconversion nanoparticles for pH-activated and near-infrared-triggered photodynamic therapy of deep tumors. *Adv. Mater.* **30**, 1802808 (2018).
6. Kim, M. M. & Darafsheh, A. Light sources and dosimetry techniques for photodynamic therapy. *Photochem. Photobiol.* **96**, 280–294 (2020).
7. Li, X., Lovell, J. F., Yoon, J. & Chen, X. Clinical development and potential of photothermal and photodynamic therapies for cancer. *Nat. Rev. Clin. Oncol.* **17**, 657–674 (2020).
8. Chen, Q. et al. Photodynamic therapy guidelines for the management of oral leucoplakia. *Int. J. Oral. Sci.* **11**, 14 (2019).
9. Bansal, A. et al. In vivo wireless photonic photodynamic therapy. *Proc. Natl Acad. Sci. USA* **115**, 1469–1474 (2018).
10. Yamagishi, K. et al. Tissue-adhesive wirelessly powered optoelectronic device for metronomic photodynamic cancer therapy. *Nat. Biomed. Eng.* **3**, 27–36 (2019).
11. Liu, Z. et al. Human motion driven self-powered photodynamic system for long-term autonomous cancer therapy. *ACS Nano* **14**, 8074–8083 (2020).
12. Shin, D. et al. The effects of low irradiance long duration photochemical internalization on glioma spheroids. *Photodiagn. Photodyn.* **26**, 442–447 (2019).
13. Larson, C. et al. Highly stretchable electroluminescent skin for optical signaling and tactile sensing. *Science* **351**, 1071–1074 (2016).
14. Lee, B. et al. Ultraflexible and transparent electroluminescent skin for real-time and super-resolution imaging of pressure distribution. *Nat. Commun.* **11**, 663 (2020).
15. Shi, X. et al. Large-area display textiles integrated with functional systems. *Nature* **591**, 240–245 (2021).
16. Sim, J. H. et al. OLED catheters for inner-body phototherapy: a case of type 2 diabetes mellitus improved via duodenal photobiomodulation. *Sci. Adv.* **9**, eadh8619 (2023).
17. Jang, J. H. et al. Materials, device structures, and applications of flexible perovskite light-emitting diodes. *Adv. Electron. Mater.* **9**, 2201271 (2023).
18. Zuo, Y. et al. Flexible color-tunable electroluminescent devices by designing dielectric-distinguishing double-stacked emissive layers. *Adv. Funct. Mater.* **30**, 2005200 (2020).
19. Lee, S. W. et al. 3D motion tracking display enabled by magneto-interactive electroluminescence. *Nat. Commun.* **11**, 6072 (2020).
20. Dinh Xuan, H. et al. Super stretchable and durable electroluminescent devices based on double-network ionogels. *Adv. Mater.* **33**, 200884 (2021).
21. Yang, Z., Wang, W., Pan, J. & Ye, C. Alternating current electroluminescent devices with inorganic phosphors for deformable displays. *Cell Rep. Phys. Sci.* **1**, 100213 (2020).
22. Wang, L. et al. Advances in alternating current electroluminescent devices. *Adv. Opt. Mater.* **7**, 1801154 (2019).
23. Yu, S. et al. Recent progress in AC-driven organic and perovskite electroluminescent devices. *ACS Photon.* **9**, 1852–1874 (2022).
24. Jiang, D. et al. Emerging implantable energy harvesters and self-powered implantable medical electronics. *ACS Nano* **14**, 6436–6448 (2020).
25. Xu, W. et al. A droplet-based electricity generator with high instantaneous power density. *Nature* **578**, 392–396 (2020).
26. Zhao, X., Askari, H. & Chen, J. Nanogenerators for smart cities in the era of 5G and Internet of Things. *Joule* **5**, 1391–1431 (2021).
27. Liu, R., Wang, Z. L., Fukuda, K. & Someya, T. Flexible self-charging power sources. *Nat. Rev. Mater.* **7**, 870–886 (2022).

28. Wu, M. et al. Stretchable freezing-tolerant triboelectric nanogenerator and strain sensor based on transparent, long-term stable, and highly conductive gelatin-based organohydrogel. *Nano Energy* **95**, 106967 (2022).

29. Zhu, S. et al. High-performance triboelectric nanogenerator powered flexible electroluminescence devices based on patterned laser-induced copper electrodes for visualized information interaction. *Nano Energy* **96**, 107116 (2022).

30. Jia, M. et al. Tactile tribotronic reconfigurable p-n junctions for artificial synapses. *Sci. Bull.* **67**, 803–812 (2022).

31. Barman, S. R. et al. A self-powered multifunctional dressing for active infection prevention and accelerated wound healing. *Sci. Adv.* **9**, adc8758 (2023).

32. Yang, P. et al. Radical anion transfer during contact electrification and its compensation for charge loss in triboelectric nanogenerator. *Matter* **6**, 1295–1311 (2023).

33. Liu, X. et al. Alternating current electroluminescent device powered by triboelectric nanogenerator with capacitively driven circuit strategy. *Adv. Funct. Mater.* **32**, 2106411 (2022).

34. Zhu, Y. et al. Wearable, freezing-tolerant, and self-powered electroluminescence system for long-term cold-resistant displays. *Nano Energy* **98**, 107309 (2022).

35. Zhang, S. et al. Wearable integrated self-powered electroluminescence display device based on all-inone MXene electrode for information encryption. *Adv. Funct. Mater.* **33**, 2307609 (2023).

36. Wangoye, K. et al. Chronic wound isolates and their minimum inhibitory concentrations against third generation cephalosporins at a tertiary hospital in Uganda. *Sci. Rep. -UK* **12**, 1195 (2022).

37. Saghazadeh, S. et al. Drug delivery systems and materials for wound healing applications. *Adv. Drug Deliv. Rev.* **127**, 138–166 (2018).

38. Ma, C.-H. et al. Intratumoral photosensitizer delivery and photodynamic therapy. *Nano Life* **11**, 2130003 (2021).

39. Maleki, A. et al. Multifunctional photoactive hydrogels for wound healing acceleration. *ACS Nano* **15**, 18895–18930 (2021).

40. Yang, S. et al. A smart DNA hydrogel enables synergistic immunotherapy and photodynamic therapy of melanoma. *Angew. Chem. Int. Ed.* **63**, e202319073 (2024).

41. Wang, J. et al. Extremely stretchable electroluminescent devices with ionic conductors. *Adv. Mater.* **28**, 4490–4496 (2016).

42. Zheng, Q. et al. In vivo self-powered wireless cardiac monitoring via implantable triboelectric nanogenerator. *ACS Nano* **10**, 6510–6518 (2016).

43. Chen, C. et al. 3D double-faced interlock fabric triboelectric nanogenerator for bio-motion energy harvesting and as self-powered stretching and 3D tactile sensors. *Mater. Today* **32**, 84–93 (2020).

44. Dai, K. et al. Self-powered triboelectric functional devices and microsystems in health-care applications: an energy perspective. *EnergyChem* **5**, 100109 (2023).

45. Meng, X. C. et al. Triboelectric and piezoelectric technologies for self-powered microbial disinfection. *Nano Energy* **127**, 109716 (2024).

46. Tao, K. et al. Origami-inspired electret-based triboelectric generator for biomechanical and ocean wave energy harvesting. *Nano Energy* **67**, 104197 (2020).

47. Demartis, S. et al. Nanotechnology-based rose Bengal: a broad-spectrum biomedical tool. *Dyes Pigments* **188**, 109236 (2021).

48. Chandna, S. et al. Lignin-bimetallic nanoconjugate doped pH-responsive hydrogels for laser-assisted antimicrobial photodynamic therapy. *Biomacromolecules* **21**, 3216–3230 (2020).

49. Zhang, X. & Wang, F. Recent advances in flexible alternating current electroluminescent devices. *APL Mater.* **9**, 030701 (2021).

50. Duc Loc, S. et al. Tailoring photosensitive ROS for advanced photodynamic therapy. *Exp. Mol. Med.* **53**, 495–504 (2021).

51. Tang, Y. et al. Oxygen-independent organic photosensitizer with ultralow-power NIR photoexcitation for tumor-specific photodynamic therapy. *Nat. Commun.* **15**, 2530 (2024).

52. Li, Z. et al. Synergistic lysozyme-photodynamic therapy against resistant bacteria based on an intelligent upconversion nanoplatform. *Angew. Chem. Int. Ed.* **60**, 19201–19206 (2021).

53. Zhu, Y. et al. Polycationic synergistic antibacterial agents with multiple functional components for efficient anti-infective therapy. *Adv. Funct. Mater.* **28**, 1706709 (2018).

54. Soehnlein, O., Steffens, S., Hidalgo, A. & Weber, C. Neutrophils as protagonists and targets in chronic inflammation. *Nat. Rev. Immunol.* **17**, 248–261 (2017).

55. Kalan, L. R. et al. Strain- and species-level variation in the microbiome of diabetic wounds is associated with clinical outcomes and therapeutic efficacy. *Cell Host Microbe* **25**, 641–655 (2019).

56. Li, G. et al. A small molecule HIF-1α stabilizer that accelerates diabetic wound healing. *Nat. Commun.* **12**, 3363 (2021).

57. Cai, Y. et al. Harnessing strategies for enhancing diabetic wound healing from the perspective of spatial inflammation patterns. *Bioact. Mater.* **28**, 243–254 (2023).

58. Wang, M. et al. Efficient angiogenesis-based diabetic wound healing/skin reconstruction through bioactive antibacterial adhesive ultraviolet shielding nanodressing with exosome release. *ACS Nano* **13**, 10279–10293 (2019).

59. Sies, H. & Jones, D. P. Reactive oxygen species (ROS) as pleiotropic physiological signalling agents. *Nat. Rev. Mol. Cell Biol.* **21**, 363–383 (2020).

60. Matoori, S., Veves, A. & Mooney, D. J. Advanced bandages for diabetic wound healing. *Sci. Transl. Med.* **13**, eabe4839 (2021).

## Author contributions
W.H., P.L., Q.J., and K.T. directed and supervised the whole project. J. Zhang and X. Mao contributed equally to this work. J.Z. designed and fabricated the system, and evaluated the data. J.Z., Q.J., and P.L. wrote the manuscript together. J.Z. and R.N. performed the in vivo experiments. X.Mao, Y.G., K.T., and H.C. helped in the construction of the triboelectric nanogenerator. All authors reviewed the manuscript.

## Competing interests
The authors declare no competing interests.

## Additional information
**Supplementary information** The online version contains supplementary material available at https://doi.org/10.1038/s41528-024-00345-9.

**Correspondence** and requests for materials should be addressed to Qingyan Jia, Kai Tao, Peng Li or Wei Huang.

**Reprints and permissions information** is available at http://www.nature.com/reprints

**Publisher's note** Springer Nature remains neutral with regard to jurisdictional claims in published maps and institutional affiliations.